ACS APPLIED MATERIALS & INTERFACES

www.acsami.org

Research Article

Carbon-Doped $TiNb_2O_7$ Suppresses Amorphization-Induced Capacity Fading

Woowon Chung and Jin Ho Bang*

Cite This: *ACS Appl. Mater. Interfaces* 2022, 14, 19365−19375

Read Online

ACCESS | Metrics & More | Article Recommendations | Supporting Information

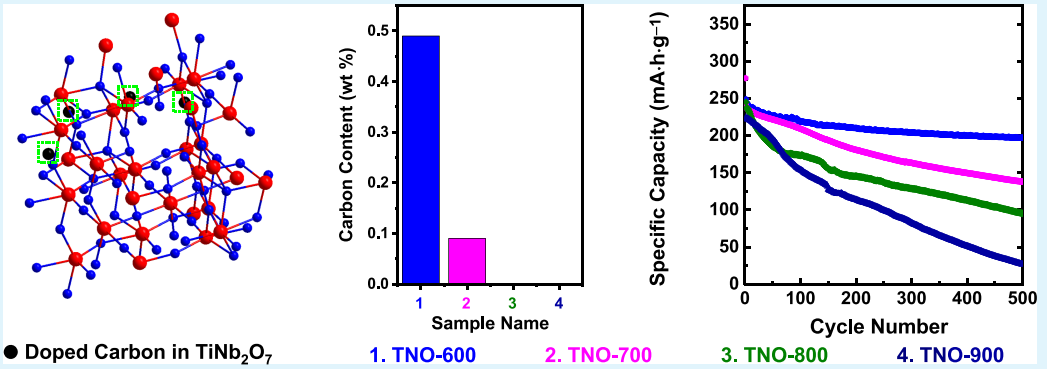

ABSTRACT: The limited capacity of graphite anodes in high-performance batteries has led to considerable interest in alternative materials in recent years. Due to its high capacity, titanium niobium oxide ($TiNb_2O_7$, TNO) with a Wadsley−Roth crystallographic sheared structure holds great promise as a next-generation anode material, but a comprehensive understanding of TNO's electrochemical behavior is lacking. In particular, the mechanism responsible for the capacity fading of TNO remains poorly elucidated. Given its metastable nature (as an entropy-stabilized oxide) and the large volume change in TNO upon lithiation and delithiation, which has long been overlooked, the factors governing capacity fading warrant investigation. Our studies reveal that the structural weakness of TNO is fatal to the long-term cycling stability of TNO and that the capacity fading of TNO is driven by amorphization, which results in a significant increase in impedance. While nanostructuring can kinetically boost lithium intercalation, this benefit comes at the expense of capacity fading. Carbon doping in TNO can effectively suppress the critical impedance increase despite the amorphization, providing a possible remedy to the stability issue.

KEYWORDS: *titanium niobium oxide, lithium-ion batteries, capacity degradation, amorphization, carbon doping*

1. INTRODUCTION

Advanced electrode materials are of great importance to the development of lithium-ion battery (LIB) technologies.[1] Novel electrode materials have provided important breakthroughs to many technical issues during the commercialization of LIBs and subsequent advances. The seminal works by the winners of the 2019 Nobel Prize for Chemistry (Whittingham, Goodenough, and Yoshino)[2] for their contributions involving novel electrode materials (e.g., $LiCoO_2$ and graphite) are prime examples. Graphite, one of the few materials successfully applied to commercially available LIB anodes, is now proving challenging to apply to high-performance systems[3] as the LIB market expands to include electric vehicles and energy storage. Graphite cannot meet the stringent requirements of high-performance applications, and significant efforts have been made to replace graphite with novel materials. Lithium titanium oxide (LTO, $Li_4Ti_5O_{12}$) is another anode material that has been commercialized,[4,5] but it suffers from a low capacity of 175 mAh g^{-1}—half of that of graphite—and poor electrical conductivity. In 2011, the Goodenough group[6,7] proposed titanium niobium oxide (TNO, $TiNb_2O_7$) with a Wadsley−Roth crystallographic sheared structure and a higher specific capacity of 388 mAh g^{-1} as a more energy-dense alternative to LTO. Since then, many other TNO analogs, such as $Ti_2Nb_{10}O_{29}$, $TiNb_6O_{17}$, $TiNb_{24}O_{62}$, and $TiNbO_4$, have been introduced.[8−10] Promising results have also been reported for TNO, and its analogs, tungsten- and niobium-based larger block phases ($W_5Nb_{16}O_{55}$ and $W_8Nb_{18}O_{69}$),[11,12] are raising more interest in Wadsley−Roth materials as alternatives to graphite.

Received: January 11, 2022
Accepted: April 12, 2022
Published: April 23, 2022

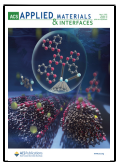

https://doi.org/10.1021/acsami.2c00589
ACS Appl. Mater. Interfaces 2022, 14, 19365−19375

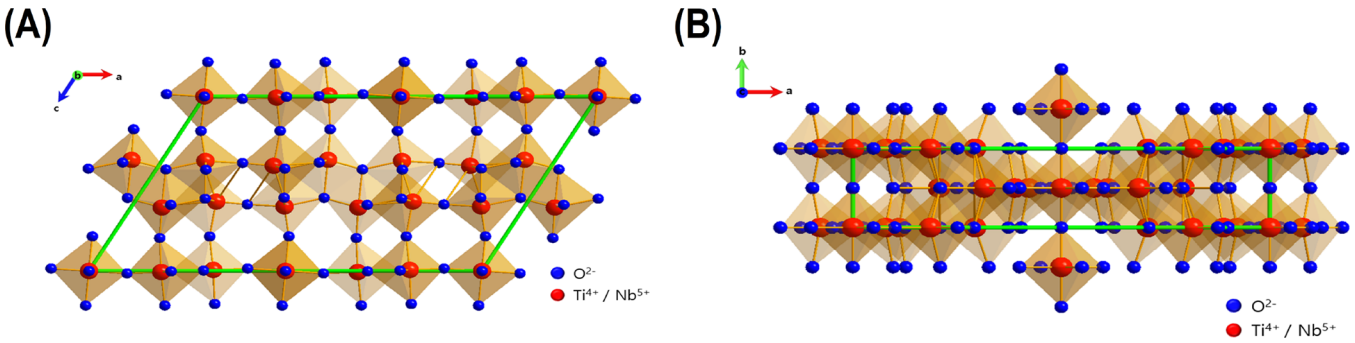

Figure 1. Crystalline structure of TNO viewed along (A) the *b* axis and (B) the *c* axis.

While the development history of TNO is relatively short, many of its structural and electrochemical properties have been revealed. TNO belongs to the *C*2/*m* space group and possesses a monoclinic shear ReO_3 structure, with shear planes composed of 3 × 3 octahedrons (MO_6; M = Ti or Nb) interconnected along the *b* axis by corner-sharing and assembled into ReO_3-like blocks (Figure 1).[8] In this unique structure, long-range one-dimensional lithium diffusion is known to occur, which is somewhat surprising when compared with another one-dimensional lithium conductor, $LiFePO_4$. Grey and co-workers recently revealed that lithium ions can diffuse through four parallel *b*-axis tunnels defined by the spatial gap between the shear planes and can also traverse tunnels with moderately low diffusion barriers.[13] Reversible lithium intercalation and deintercalation are believed to occur repeatedly as the corner-shared ReO_3 framework associated with edge-sharing gives TNO sufficient structural robustness against structural distortion.[9] Although TNO itself is electrically neutral due to the presence of the d^0 state resulting from the oxidation states of niobium and titanium (Nb^{5+} and Ti^{4+}), as with Nb_2O_5,[14] it can be transformed into an electrical conductor upon lithiation.[13] However, low ionic conductivity, particularly in highly lithiated states, is still a technical challenge preventing the development of an efficient TNO lithium storage host.[13] A wide variety of TNO nanostructuring strategies have been explored to shorten the diffusion length, as summarized in a recent review.[8] Another benefit from nanoscaling is the additional capacity resulting from pseudocapacitive charge storage.[15]

Despite the merits of nanostructures, their undesirable effects should not be overlooked. Nanostructuring can kinetically boost lithium intercalation (thus improving the LIB performance of TNO),[8,16] but the increased surface area can inevitably undermine stability. However, little attention has been made to this important issue to date. In addition, two important characteristics of TNO have been overlooked and may pose a great threat to nanostructured TNOs. First, TNO is structurally metastable. Because it is an entropy-stabilized oxide due to its positive formation enthalpy (3.86 ± 1.9 kJ mol^{-1}),[17] TNO can be synthesized at high temperatures to compensate for unfavorable energetics, and the crystal structure of TNO can be retained only because of kinetic constraints against decomposition.[17] Second, TNO experiences a large volume change of 8−10% upon lithiation and delithiation,[18,19] which makes it vulnerable to mechanical damage. As with $LiNiO_2$ and its families,[20,21] such a vulnerability to mechanical fracture would be critical in any attempt to sustain structural integrity over long-term operations. We explored these overlooked aspects of nanostructured TNO. As we speculated, nanostructured TNO indeed lost its capacity gradually upon repeated charging and discharging, and this capacity fading can be attributed primarily to the amorphization that results from continual grain fracturing. Another important finding of this work is that carbon doping of TNO can significantly suppress the fading of capacity associated with amorphization. An in-depth electrochemical impedance spectroscopy (EIS) analysis revealed that the doped carbon plays a pivotal role in maintaining the initial charge transfer resistance and solid-state lithium diffusivity, allowing for capacity retention despite the detrimental amorphization.

2. EXPERIMENTAL SECTION

2.1. Synthesis of $TiNb_2O_7$ Nanospheres. Nanospheres of $TiNb_2O_7$ were prepared using a two-step process: a sol−gel reaction and subsequent calcination of the obtained sol−gel reaction product. For the sol−gel reaction, 40 mL of ethylene glycol (99.5%, Daejung Chemical & Metal Co., Ltd.) was poured into a 300 mL round-bottom flask in a nitrogen-filled glove box. Titanium butoxide (97%) and niobium ethoxide (99.999%) purchased from Merck with a molar ratio of 1:2 were added to the flask under stirring. The solution was mixed for 30 min, and an aliquot of acetone (99.95%, Daejung Chemical & Metal Co., Ltd.) in deionized water (1 mL of acetone in 99 mL of deionized water) was then rapidly injected into the solution to initiate the sol−gel reaction. The obtained white precipitate was thoroughly washed with deionized water and ethanol several times and dried at 60 °C in an oven. To synthesize $TiNb_2O_7$ nanospheres, this dried precursor was weighed out into an alumina crucible and placed in a muffle furnace with a temperature elevated to a target temperature (550, 600, 700, 800, and 900 °C) at a ramping rate of 10 °C min^{-1}. Calcination in air at each target temperature was carried out for 2 h. The samples will hereafter be referred to as TNO-550, TNO-600, TNO-700, TNO-800, and TNO-900.

2.2. Material Characterization. Crystal structural information of the TNO samples was obtained using an X-ray diffractometer (Bruker D2 PHASER) with Cu *Kα* (1.5406 Å) irradiation operating at 10 mA and 30 kV. The surface area and porous nature of TNO were examined using a surface area analyzer (BELSORP-mini II, BEL Japan). Nitrogen physisorption isotherms were measured at 77 K, and the specific surface area and pore-size distributions were determined using the Brunauer−Emmett−Teller (BET) and Barrett−Joyner−Halenda (BJH) methods, respectively. Microstructural characteristics were examined using scanning electron microscopy (SEM, Hitachi S-4800) and transmission electron microscopy (TEM, JEOL-2100F). Thermogravimetric analysis (TGA) and differential scanning calorimetry (DSC) analysis were carried out with a thermal analyzer (SDT-Q600, TA Instrument) at a healing rate of 10 °C min^{-1} under airflow. Fourier transform infrared (FT-IR) spectroscopy (Spectrum Two, PerkinElmer) and Raman spectroscopy (Renishaw RM-1000) were performed to obtain the structural information occurring during the calcination. X-ray photoelectron spectroscopy (XPS, PHI Versa

https://doi.org/10.1021/acsami.2c00589
ACS Appl. Mater. Interfaces 2022, 14, 19365−19375

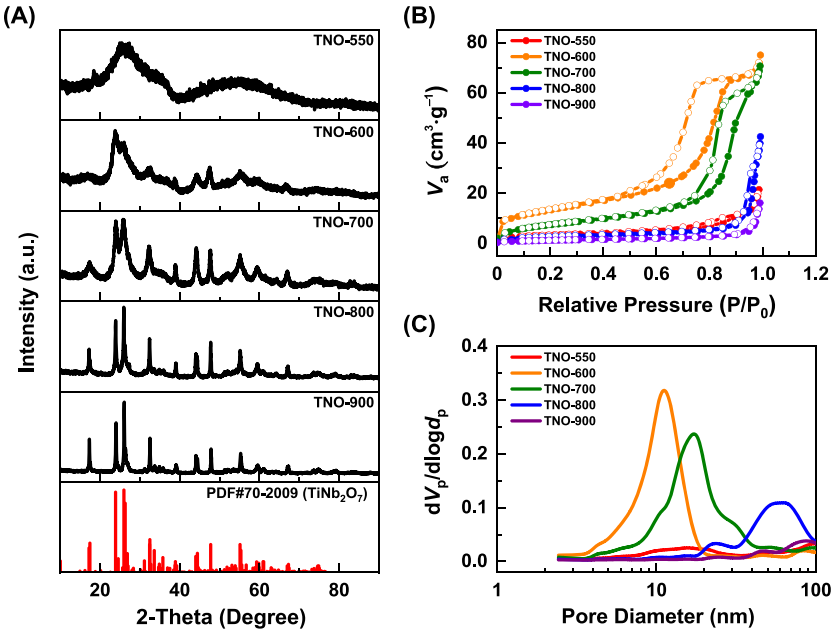

Figure 2. (A) XRD patterns of TNO samples. (B) N_2 physisorption isotherms and (C) the BJH plot of TNO samples.

Table 1. Lattice Parameters, Grain Size, Specific Surface Area, and the Carbon Content of Each TNO

	lattice parameter (Å)						
sample	*a*	*b*	*c*	grain size (nm)	surface area ($m^2\ g^{-1}$)	total pore volume ($cm^3\ g^{-1}$)	carbon amount (wt %)
TNO-600	11.780	3.818	20.455	4.4	47.8	0.114	0.42
TNO-700	11.892	3.808	20.473	6.0	30.7	0.120	0.09
TNO-800	11.960	3.809	20.423	21.2	8.1	0.069	0
TNO-900	11.940	3.805	20.412	33.9	4.6	0.025	0

Probe system) was carried out to examine the surface charge state of the TNO samples.

2.3. Electrochemical Analysis. To explore the electrochemical behavior of the TNO nanospheres, half-cells based on a CR-2032-type coin cell were fabricated in an argon-filled glove box. A slurry containing an active material (each TNO sample), carbon black (Super P), and polyvinylidene difluoride binder dissolved in *N*-methyl-2-pyrrolidone at a weight ratio of 8:1:1 was prepared using a planetary centrifugal mixer (AR-100, THINKY Corp.). With a micrometer-scale adjustable film applicator, the slurry was applied and spread evenly onto copper foil, and the resulting film was dried for 12 h in a vacuum oven at 120 °C. The total loading amount of the TNO sample was ~1.0 mg cm^{-1}. For the coin-cell fabrication, lithium foil, a Celgard 2320 membrane, and 1 M lithium hexafluorophosphate dissolved in ethylene carbonate/dimethyl carbonate (1:1 ratio) were used, and all these components along with the electrode prepared above were properly assembled and aged for 24 h before any electrochemical tests. Battery cyclers (WBCS3000, WonATech Co., Ltd.) were employed to perform galvanostatic charge/discharge measurements, cyclic voltammetry (CV), and galvanostatic intermittent titration technique (GITT) analysis, with 1C being defined as 388 mAh g^{-1}. A ZIVE BP2A electrochemical workstation (WonATech Co., Ltd.) was used for EIS analysis performed under a perturbation amplitude of 10 mV in a range of 0.001 Hz to 10 kHz.

3. RESULTS AND DISCUSSION

3.1. Characterization of TNO Obtained from the Ti-Nb-Glycolate Precursor. For the synthesis of nanostructured TNO, an organic−inorganic hybrid precursor based on Ti-Nb-glycolate prepared by the sol−gel reaction was employed. The sol−gel reaction has proven useful in the preparation of this kind of precursor because the structural integrity of the organic moiety that dictates the formation of nanostructures can be sustained without being decomposed.[22−25] Upon calcination in air, the organic part of the precursors burns out, acting as porogens, while the remaining inorganic part turns into oxides. Figure 2A displays the X-ray diffraction (XRD) patterns of TNOs obtained at different calcination temperatures. At 550 °C, TNO was largely amorphous, but beginning at 600 °C, TNO turned into a crystalline material with diffraction peaks corresponding to those of standard TNO (JCPDS 70-2009). As suggested by the appearance of more sharpened, intense diffraction peaks, as temperatures rose, the crystalline nature was enhanced when the calcination temperature increased. A noticeable change in the peak width was observed when the temperature was increased from 700 to 800 °C, implying that grain growth was accelerated in this temperature range. This speculation was confirmed by the grain-size trend produced by the Scherrer equation (Table 1). The average grain size of TNO-700 was just 6.0 nm, but it increased to 21.2 nm for TNO-800. Lattice parameters were also determined by the Rietveld refinement analysis (Table 1), with a systematic decrease in the lattice parameter *b* from 3.818 to 3.805 Å when the calcination temperature increased from 600 to 900 °C. Given the lithium intercalation channels in TNO, it was anticipated that TNO-600 would provide a more favorable environment for lithium diffusion than other counterparts. Figure 2B depicts the N_2 physisorption isotherms of each TNO. Unlike TNO-550, which produced a type III-like isotherm with reversible curvature (i.e., nonporous), the isotherms of TNO-600 and TNO-700 featured type IV isotherms with a type H2 hysteretic loop, indicating the

https://doi.org/10.1021/acsami.2c00589
ACS Appl. Mater. Interfaces 2022, 14, 19365−19375

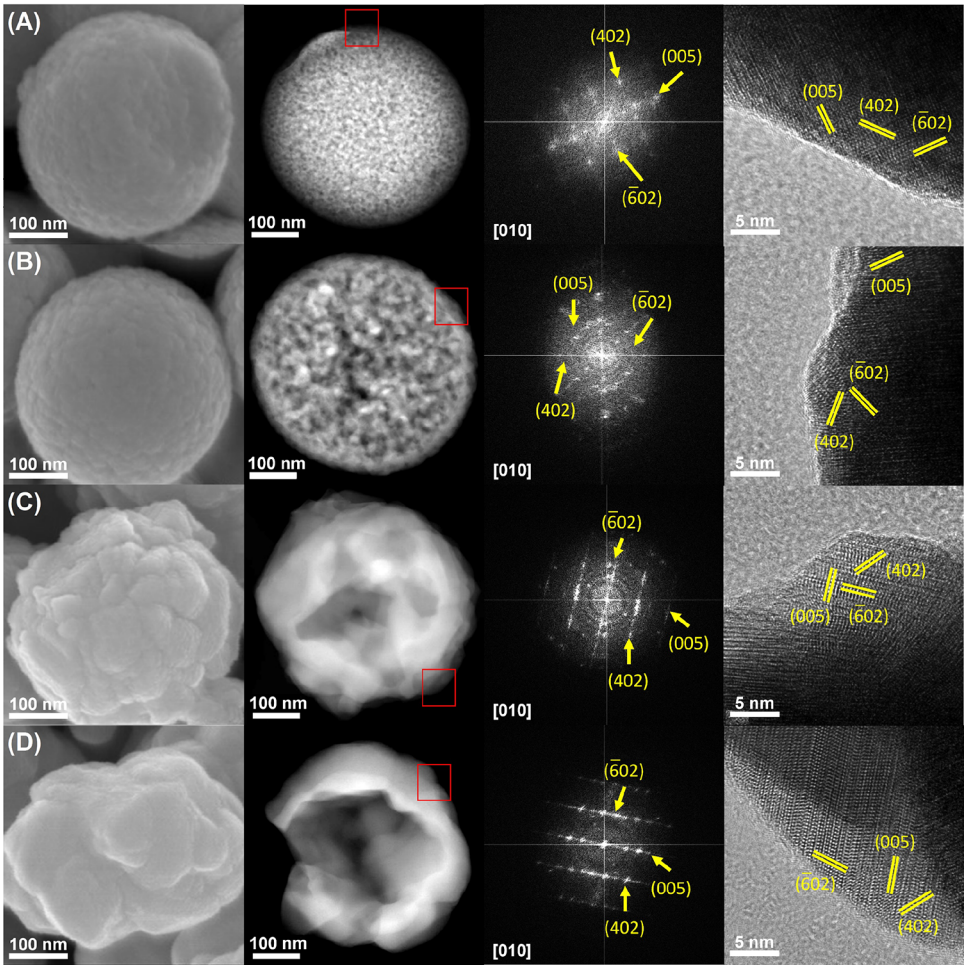

Figure 3. SEM images, TEM dark-field images, FFT patterns, and HRTEM images of (A) TNO-600, (B) TNO-700, (C) TNO-800, and (D) TNO-900.

development of randomly distributed mesopores.[23] However, the isotherms for TNO-800 and TNO-900 reverted to type III-like in nature, suggesting that a dramatic morphological change occurred between temperatures of 700 and 800 °C. This observation was in close agreement with the notable change observed in the XRD analysis and reflected in the trend of the BET specific surface area (Table 1) and the pore-size distribution (Figure 2C). The surface areas of TNO-600 and TNO-700 were as large as 47.8 and 30.7 $m^2 g^{-1}$, respectively, with total pore volumes of 0.114 and 0.120 $cm^3 g^{-1}$, respectively, whereas TNO-800 and TNO-900 exhibited respective surface areas of just 8.1 and 4.6 $m^2 g^{-1}$, with total pore volumes of 0.069 and 0.025 $cm^3 g^{-1}$, respectively. While a multimodal mesoporous structure appeared prominently in TNO-600 and TNO-700, the porous nature faded out in the case of TNO-800 and TNO-900.

Microstructural information of the TNO samples was obtained using electron microscopy (Figure 3). The TNO precursor was spherical, with an average diameter of ~400 nm (Figure S1), and this spherical morphology was largely retained even after calcination. However, depending on the temperature, surface roughness became more prominent, presumably due to the complete decomposition of the organic part and the rapid grain growth. The TEM imaging revealed the formation of a porous structure in TNO-600 and TNO-700 and the evolution of porous TNO to hollow TNO as temperatures rose. Consistent with the BJH plot, most of the pores that developed in TNO-600 were less than 10 nm in diameter and the presence of small crystallites was supported by a poorly developed fast Fourier transform (FFT) pattern. With elevated temperatures, grains began to grow, accompanied by the merging of nanopores into larger mesopores (TNO-700) and eventually into a hollow cavity (TNO-800 and TNO-900). The FFT patterns became more prominent, and the lattice fringes in high-resolution TEM (HRTEM) images were also more visible in TNO-900 than other counterparts, reflecting the rapid crystallite growth at this temperature. A dramatic morphological change from a porous to a hollow structure was observed when the temperature was increased from 700 to 800 °C, which is consistent with the sudden grain growth observed in the XRD analysis and the sharp decrease in the BET surface area. We speculated that the microstructural changes (nanoporous-to-hollow spheres) occurring during the heat treatment at different temperatures are closely related to a new hollowing mechanism called "shell-induced Ostwald ripening", which was recently reported.[26] According to this mechanism, small crystallites formed inside TNO-600 begin to dissolve because of high surface energy and they can be redeposited on the inner surface of the relatively stable outer shell. The growth of the shell continues at the expense of small crystallites until a thick, stable layer is formed.

https://doi.org/10.1021/acsami.2c00589
ACS Appl. Mater. Interfaces 2022, 14, 19365−19375

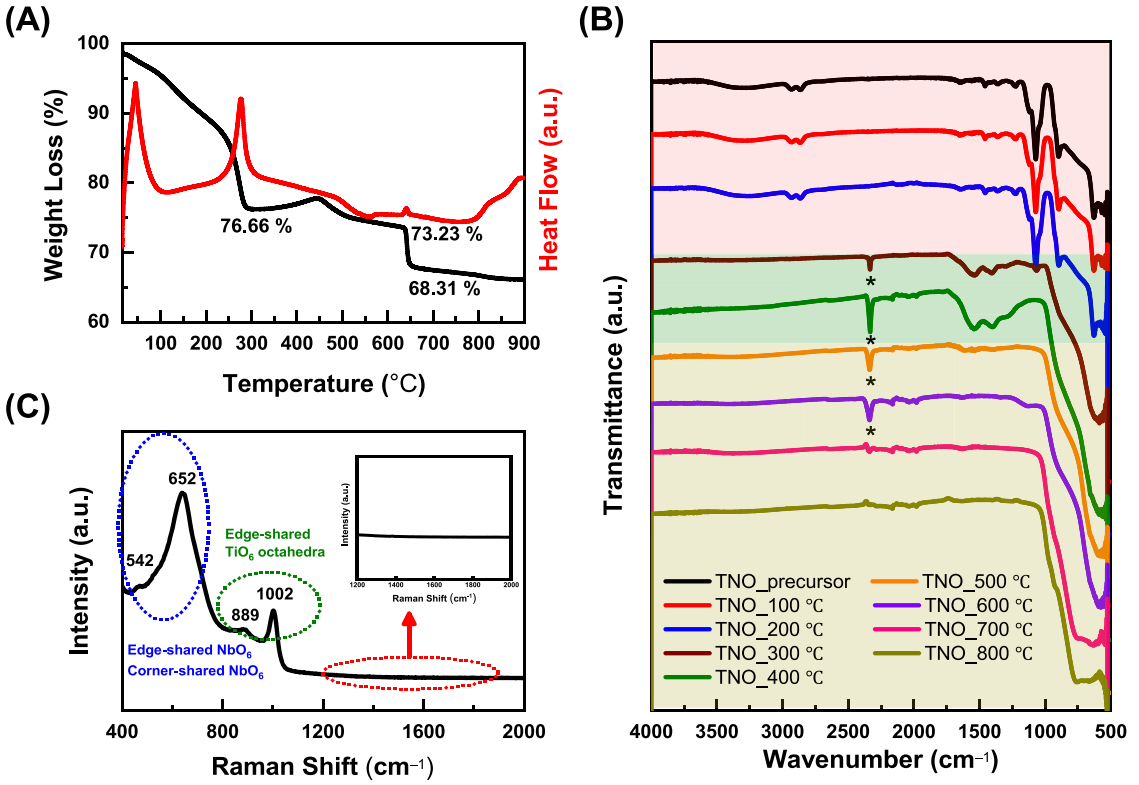

Figure 4. (A) TGA analysis of the TNO precursor and (B) FT-IR spectra of the TNO precursor at various temperatures. The peak labeled by an asterisk originated from CO_2 in air. (C) Raman spectra of TNO-600. The inset shows the enlarged spectrum in the region of the Raman shift between 1200 and 1800 cm^{-1}, revealing that no carbon network was formed in TNO.

More insight into the mechanistic steps that led to the microtextual transformation was obtained from TGA and DSC analyses (Figure 4A). The initial weight loss seen until ~170 °C was associated with the loss of water that had been physisorbed and/or bound to the glycolate, and the subsequent weight loss observed up to ~300 °C can be attributed to the decomposition of the TNO precursor.[27] Weight gain was observed between 350 and 550 °C, and when the temperature reached ~650 °C, another noticeable weight loss was observed followed by gradual weight loss. As revealed by FT-IR spectra (Figure 4B), the spectral features of the TNO precursor and those of TNO heated at 300 °C were noticeably different, confirming that 300 °C was the onset temperature of TNO decomposition. Also, FT-IR analysis revealed that the weight gain from ~350 °C was associated with the formation of oxygen-functionalized residual carbon. Based on the carbon content of TNO-600, it appeared that the decomposition of the TNO precursor at approximately 300 °C cannot completely burn ethylene glycolate units out of the TNO precursor. Some of it may have turned into oxygen-functionalized carbon, which is associated with broad peaks appearing at wavenumbers of 1000−1750 cm^{-1} when the temperature was being raised. However, the spectral feature associated with the oxygen-functionalized carbon gradually disappeared as temperatures increased and completely vanished at 800 °C. We speculated that the weight loss evident at ~650 °C in the TGA analysis can be ascribed to the residual carbon burning out of TNO; this was partly supported by the results of elemental analysis (Table 1). The amounts of carbon in TNO-600 and TNO-700 were 0.42 and 0.09 wt %, respectively, but no carbon was detected in the TNO-800 and TNO-900 samples. The presence of carbon was also indicated by the color of each TNO sample (Figure S2), with a slightly yellow color in TNO-600 gradually disappearing and TNO turning white when calcined above 800 °C. The nature of the carbon in TNO-600 and TNO-700 was investigated by Raman spectroscopy (Figure S3). The Raman spectrum of TNO-600 showed no characteristic Raman peaks (i.e., D and G bands) that correspond to disordered and ordered carbon networks (Figure 4C). As shown in Figure 4C, only characteristic peaks associated with vibrational modes of NbO_6 and TiO_6 octahedra were observed at the Raman shift below 1000 cm^{-1}.[28] It is worth noting that weak peaks corresponding to the D and G bands appeared in the case of TNO-550 (Figure S4) presumably because of a greater amount of carbon doping (1.16 wt %) than TNO-600. As previously demonstrated,[29] the absence of the D and G bands suggests that carbon was present in the TNO lattice as a dopant, not as independent carbon layers. The carbon doping was also indirectly evidenced by XPS analysis. The doped carbon would inevitably affect the charge balance of a parent oxide (i.e., TNO), which often appeared as a peak shift to the lower binding energy in XPS spectra.[30] In accordance with the previous reports,[29−31] our TNO samples showed the same trend in the XPS analysis. A peak shift to the lower binding energy with respect to those of TNO-800 and TNO-900 that possess no carbon was observed in the XPS Ti 2p and Nb 3d spectra of TNO-600 and TNO-700 (Figure S5), which was attributed to the presence of doped carbon incorporated into the TNO lattice.

3.2. Electrochemical Analysis of TNO. The electrochemical behavior of each TNO during lithium intercalation and deintercalation was investigated using CV, which is a simple but intuitive analytical method through which the charge storage mechanism can be glimpsed. According to

https://doi.org/10.1021/acsami.2c00589
ACS Appl. Mater. Interfaces 2022, 14, 19365−19375

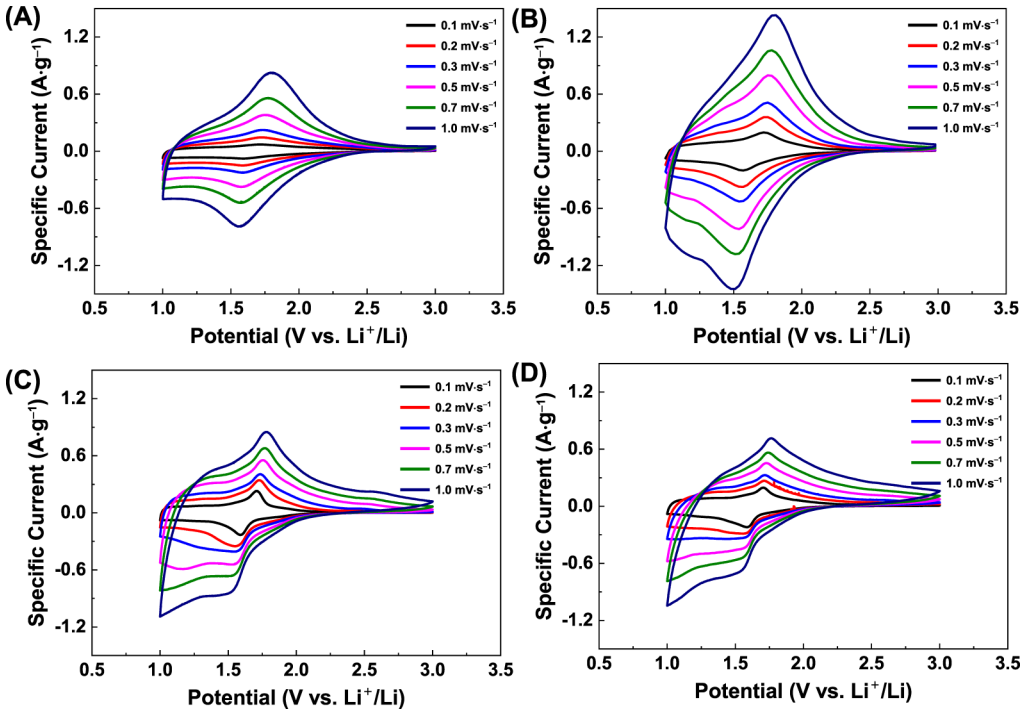

Figure 5. Cyclic voltammograms at different scan rates of (A) TNO-600, (B) TNO-700, (C) TNO-800, and (D) TNO-900.

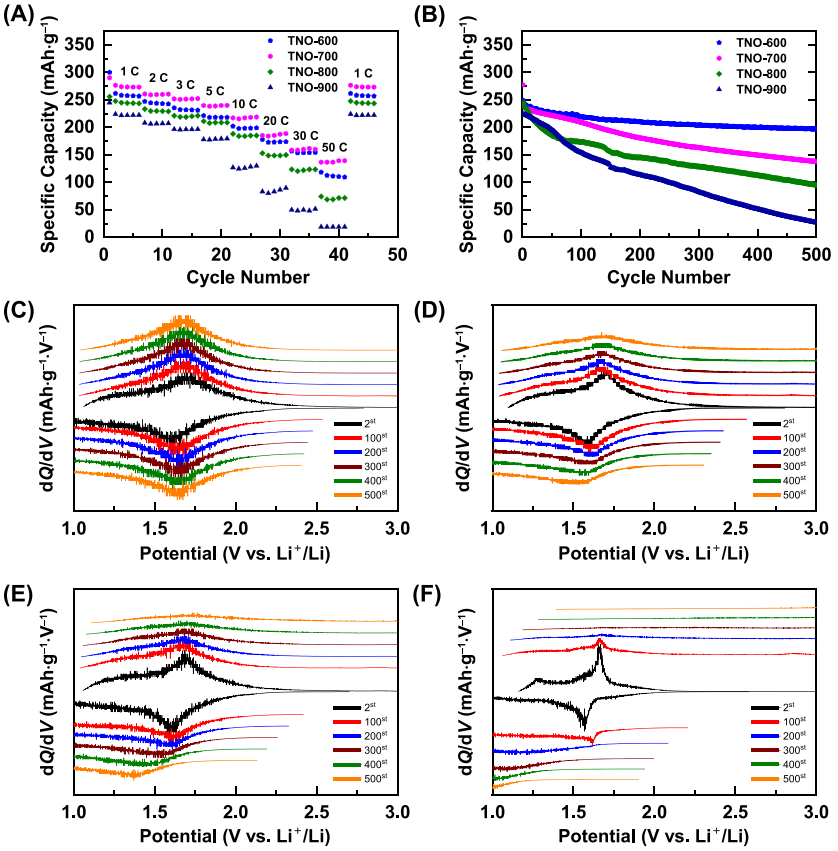

Figure 6. (A) Rate capabilities and (B) cycling stability of each TNO. Differential capacity ($dQ\ dV^{-1}$) plots corresponding to different cycle sequences in the long-term test: (C) TNO-600, (D) TNO-700, (E) TNO-800, and (F) TNO-900. To improve visibility, the plots in each figure were offset.

previous *in situ* XRD analysis results,[32] lithium intercalation and deintercalation in TNO proceed through two solid-solution and one bi-phase transition processes. During lithium intercalation, $TiNb_2O_7$ first incorporates lithium ions by forming $Li_{0.88}TiNb_2O_7$ without the phase transition, $Li_{0.88}TiNb_2O_7$ subsequently transforms into $Li_{2.67}TiNb_2O_7$

https://doi.org/10.1021/acsami.2c00589
ACS Appl. Mater. Interfaces 2022, 14, 19365−19375

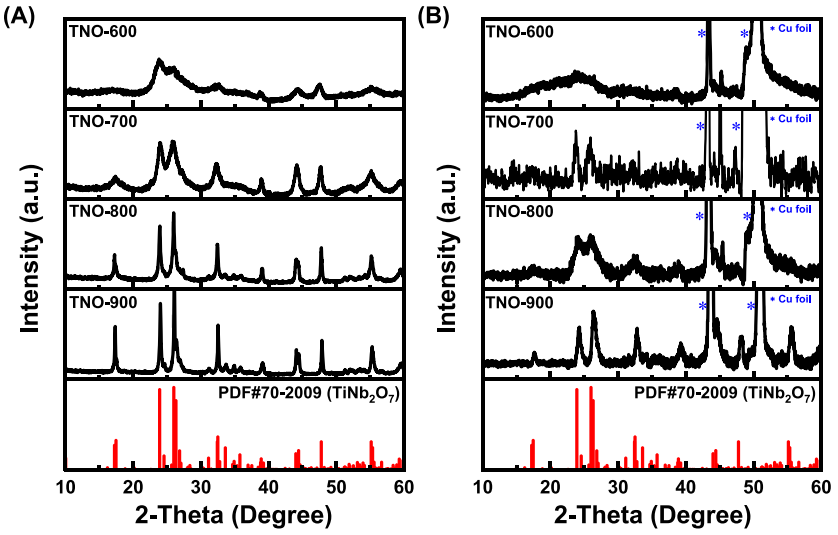

Figure 7. XRD patterns of each TNO measured (A) before and (B) after the long-term cycling test.

through a two-phase reaction (i.e., a bi-phase transition), and $Li_{2.67}TiNb_2O_7$ finally evolves to fully lithiated $Li_4TiNb_2O_7$ via a solid-solution route.[8] Given this mechanism, we anticipated that broad redox peaks associated with a sharp redox peak would appear in the cyclic voltammogram. However, TNO-600 exhibited only broad redox peaks throughout the potential window. With increased temperature, a pair of sharp peaks began to appear at ~1.7 V vs Li^+/Li (Figure 5), indicating the advent of the bi-phase transition. Given this observation, TNO-600 would likely be free of the two-phase transition. It is worth noting that the complete absence of the bi-phase transition in TNO-600 cannot be fully supported only by CV experiments, given the very broad feature of the CV peak. However, it is obvious that the contribution of the bi-phase transition to the capacity is the most minimized in TNO-600 compared to other counterparts because this bi-phase transition gradually appeared for TNO samples calcined at higher temperatures. Our speculation was supported when we further analyzed the CV responses based on the power-law relationship[33]

$$i_p = a \cdot \nu^b \tag{1}$$

where i_p is the peak current (A), a and b are the parameters, and ν is the potential scan rate (mV s^{-1}). If the value of b is 1, then the charge transfer process is capacitive, and if it is 0.5, then the process is diffusion-limited. In a complex system, the value of b typically lies between 0.5 and 1.0. Figure S6 shows the plots of the logarithm of the peak current as a function of the logarithm of the scan rate. The slope of the linear line (i.e., b) was greater than 0.9 for TNO-600 and TNO-700, whereas those of TNO-800 and TNO-900 were less than 0.65. This implies that the lithium intercalation and deintercalation were primarily dictated by the capacitive mechanism in TNO-600 and TNO-700 and not limited by solid-state lithium diffusion. To further explore the pseudocapacitive nature observed in TNO-600 and TNO-700, GITT was performed to estimate the diffusion coefficients (D_{Li}) as a function of potential. The resulting diffusion coefficients were nearly identical for all four TMO electrodes (Figure S7). Given the following equation for the equilibrium time for lithium diffusion (τ_{eq}) together with the GITT results[34]

$$\tau_{eq} = \frac{L^2}{D_{Li}} \ (L\text{: particle size}) \tag{2}$$

we inferred that any difference in solid-state lithium diffusion can be attributed to the particle size (i.e., grain size). If the grain size was greater than a specific value, then lithium diffusion in TNO would begin to be diffusion-limited, as was the case for TNO-800 and TNO-900. (This is valid only in a potential range in which two-phase intercalation governs the electrochemical process.) The near absence of diffusion limitation in TNO-600 was a product of the smaller grain size and the resulting larger surface area. We, therefore, concluded that the electrochemical behavior of TNOs is governed by extrinsic pseudocapacitance.[35]

The observations made by the CV analysis were verified by galvanic discharge/charge profiles (Figure S8). Only a gradual potential decrease with no flat galvanostatic features was observed in TNO-600 and TNO-700, but a flat galvanostatic profile in which the potential barely varied with the specific capacity appeared at 1.6−1.7 V in the case of TNO-800 and TNO-900. The rate-dependent capacities of each TNO are presented in Figure 6A. The specific capacity of TNO-600 at 1C reached 273 mAh g^{-1} but that of TNO-900 was 222 mAh g^{-1}, indicating that the capacity decreased with increasing calcination temperature. Such a capacity difference became much more prominent when the C-rates were increased. While TNO-600 can sustain its capacity at values as high as 217 and 139 mAh g^{-1} at 10C and 50C, respectively, the capacities of TNO-900 at 10C and 50C were only 128 and 19 mAh g^{-1}, respectively. Given the similar diffusion coefficients in the GITT analysis, this high rate capability of TNO-600 can be attributed to the smaller crystallites that shortened the lithium diffusion distance. Another noticeable difference was observed in the long-term stability test results. Figure 6B illustrates the substantial difference in the stability of each TNO electrode (see Figure S9 for Coulombic efficiencies measured during the long-term cycling). Although there was a gradual decrease in the capacity in TNO-600, approximately 80% of its initial capacity was retained after 500 cycles. However, the capacity decrease became much more prominent in TNO samples prepared at higher temperatures. In the case of TNO-900, the irreversible capacity fading was dramatic, retaining only 11% of

https://doi.org/10.1021/acsami.2c00589
ACS Appl. Mater. Interfaces 2022, 14, 19365−19375

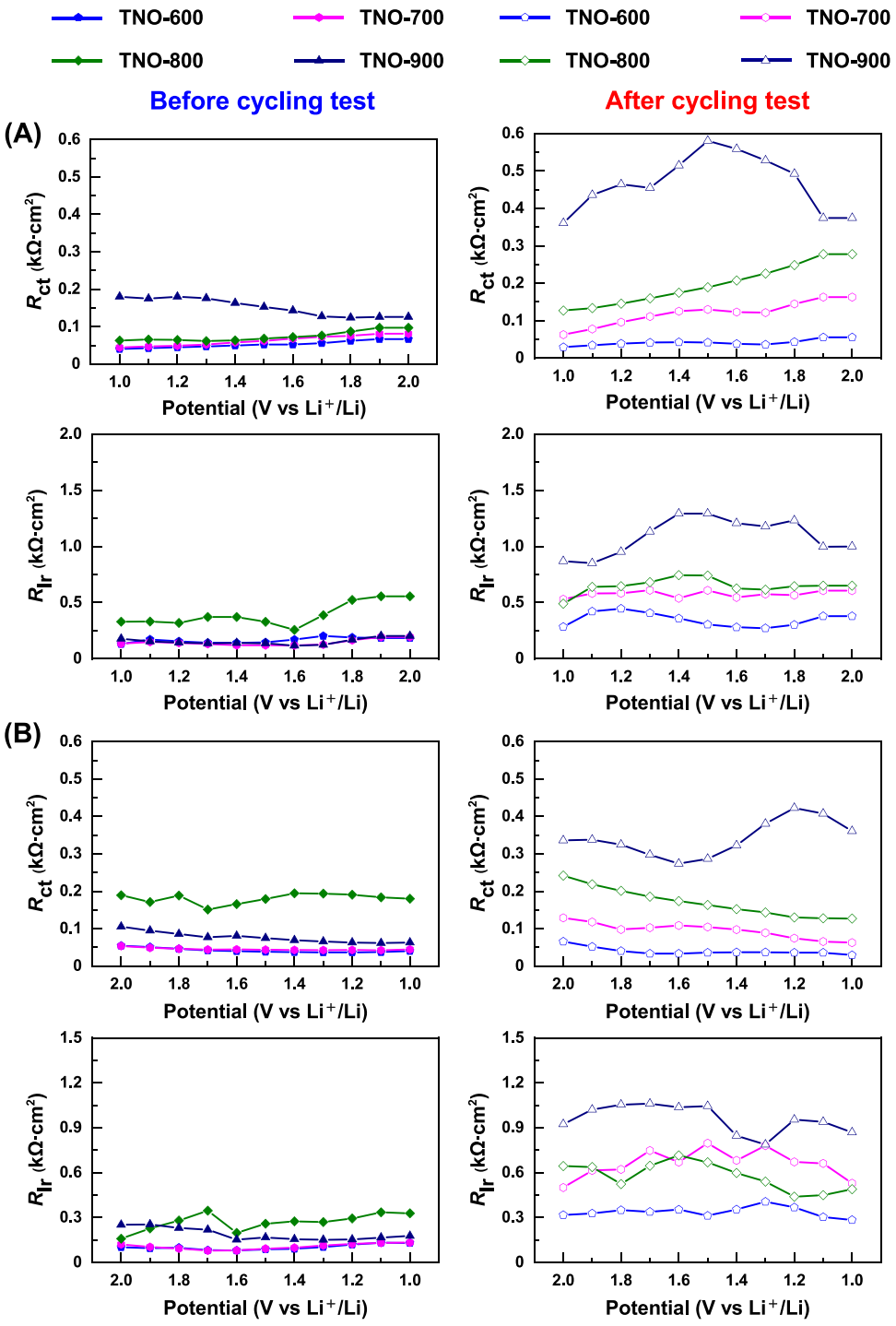

Figure 8. EIS parameters as a function of potential that are extracted from Nyquist plots taken before and after the long-term cycling test during (A) charge and (B) discharge: the interfacial charge transfer resistance (R_{ct}) and the resistance to solid-state Li diffusion (R_{lr}). Note that "before cycling" means the battery cells that went through a one-time activation process at 0.1C charge/discharge rate.

its original capacity after 500 cycles. It is worth noting that TNO-700 showed a more dramatic capacity fading than TNO-600 despite the similar charge storage mechanism and microstructural properties, suggesting that other factors (different carbon contents in particular) must have played an important role in bringing about the disparity. To shed more light on this difference in capacity fading, differential capacity ($dQ\ dV^{-1}$) analysis was performed, with the results presented in Figure 6C–F. In the case of TNO-600, no notable change was found in the overall feature (a single broad peak) over 500 cycles, implying that pseudocapacitive charge storage occurred in TNO-600 regardless of cycling numbers. As the temperature increased, the initial $dQ\ dV^{-1}$ peak sharpened in a range of 1.6–1.7 V, and the Faradic redox feature was more clearly visible in TNO-900. This suggested that the two-phase transition began to be involved in the charge storage in TNO due to the larger crystallite sizes (i.e., extrinsic pseudocapacitance). Upon repeated charge/discharge cycles, this redox feature disappeared gradually, and a noticeable transition from a diffusion-limited to a pseudocapacitive

https://doi.org/10.1021/acsami.2c00589
ACS Appl. Mater. Interfaces 2022, 14, 19365–19375

mechanism for charge storage was observed in TNO-900. Given the extrinsic pseudocapacitance of TNO, this implies that the lithium diffusion path became shortened (i.e., a decrease in grain size) during the long-term cycling. To test this hypothesis, we carried out a postmortem XRD analysis of each TNO electrode. Figure 7 reveals that severe amorphization (i.e., grain-size decrease) took place in all TNO samples during the long-term test regardless of its initial crystallinity. This observation was reaffirmed by selected area electron diffraction (SAED) patterns of all TNO electrodes taken before and after the long-term cycling (Figures S10−S13); all SAED patterns receded after the 500 cycles. For TNO-600, few diffraction peaks survived after 500 cycles, whereas most of the peaks of TNO-900 remained in the XRD pattern and their intensity significantly decreased, presumably due to grain fractures. More crystalline TNO-900 was therefore more resistant to amorphization, but this analysis made it clear that structural degradation into the amorphous phase is inevitable for the TNOs explored in this work. This result was initially puzzling because it was contradictory to the results of a study by Cava and co-workers, who found that lithium insertion/extraction in TNO barely affects the structural integrity of bulk TNO.[36] Our observation was also different from a recent demonstration of the intrinsic stability of bulk TNO over long-term cycling.[18] The reason for this disparity is unclear but may involve the close relationship between nanostructuring and capacity fading. As TNO is an entropy-stabilized oxide with a positive enthalpy of formation, its crystal structure is kinetically stabilized.[17] While nanostructuring can improve the kinetics of lithiation and delithiation, this benefit comes at the expense of stability. Given that TNO is subject to a large volume change (8−10%) unlike LTO (<0.2%), it was reasonable to assume that nanostructured TNO would suffer more than its bulk counterparts from severe mechanical damage during repeated lithiation and delithiation, which can lead to capacity degradation over cycling, as shown in Figure 6B. This revealed for the first time that amorphization is the primary reason for the capacity degradation of nanostructured TNO, which has long been overlooked in the development of the TNO material. Because amorphization appears to be unavoidable in nanostructured TNO, elucidating the failure mechanism and developing a strategy to circumvent or at least suppress the capacity fading resulting from structural degradation should be given high priority.

The remaining question was how TNO-600 can retain a useful capacity even after it completely loses its original crystallinity. Exploring the underlying reason is crucial because it may give an important hint to overcoming the overlooked stability issue of nanostructured TNO. To this end, we performed EIS analysis and compared various interfacial resistance components before and after 500 cycles. It is worth noting that the original morphology of all TNO samples was almost preserved (Figures S14−S17) according to our postmortem SEM and TEM analyses, excluding any possibility of the contribution of morphological change to impedance increment in the electrode. Figure 8 provides the various resistance components extracted from the EIS fitting of Nyquist plots measured at various potentials during the charge/discharge process. The EIS analysis was performed before and after the long-term cycling to monitor changes in interfacial resistance and solid-state diffusion resistance. Spectral features recorded during the measurements (i.e., Nyquist plots) are presented in Figures S18 and S19, and they are fitted using the equivalent circuit presented in Figure S20. A notable difference between the Nyquist plots measured before the long-term cycling test and those after the long-term cycling test was the need for an additional resistor−capacitor circuit that represented the solid-electrolyte interface (SEI) layer for the fitting. Theoretically, the formation of the SEI layer on the surface of TNO can be inhibited by high operation potential, which is greater than 1.0 V. However, Wu and co-workers recently revealed that an SEI layer can form on TNO as a result of the decomposition of an electrolyte during repeated lithiation/delithiation.[37] Indeed, the formation of the SEI layer after the long-term cycling was observed in our TNO samples (Figure S21). The resistances associated with the interfacial charge transfer (R_{ct}) and the solid-state lithium diffusion resistance (R_{lr}) measured during charging and discharging before the long-term test were nearly identical, although slightly greater resistance values were observed in TNO-800 and TNO-900. However, this resistance trend changed dramatically after the long-term test. The R_{ct} values were in the order of TNO-600 < TNO-700 < TNO-800 < TNO-900, and a noticeable increase in R_{ct} was observed in the case of TNO-900. The R_{lr} values showed a similar trend as those for R_{ct} values, and the resistance linked to the diffusion through the SEI layer (R_{SEI}) also exhibited a tendency found in the R_{ct} values (Figure S22). The capacity fading of LIB materials remains to be elucidated, but several factors are known to be involved in its origin, including the loss of crystallinity that results from mechanical damage, the consequent decrease in electrical conductivity, and the SEI growth that impedes effective lithium diffusion.[38] Our EIS analysis revealed that, despite the complete amorphization that normally leads to a drastic impedance increase, TNO-600 exhibited significantly suppressed impedance increments. This is in sharp contrast to the substantial impedance increases observed in TNO-900, although its crystalline nature was only partially damaged, unlike TNO-600. This suggests that carbon doping in TNO-600 may play a pivotal role in suppressing impedance increments, which is in close agreement with the effect of carbon doping (improving electrical conductivity and enhancing Li^+ diffusion) on the LIB performance of various anode materials in the literature.[29−31,39]

4. CONCLUSIONS

As an alternative to graphite, $TiNb_2O_7$ has received great attention as a possible anode material in LIB applications. Our exploration of the nanostructuring effect of $TiNb_2O_7$ on its electrochemical performance revealed overlooked drawbacks. Due to the metastable nature and a large volume change upon lithiation/delithiation, TNO suffers from capacity degradation over repeated cycles, and this capacity fading can be attributed to structural degradation (amorphization). A postmortem XRD analysis revealed that amorphization can be accelerated when TNO possesses a smaller grain size and a large surface area (i.e., more nanostructured). However, capacity fading resulting from amorphization can be significantly alleviated by incorporating a small amount of carbon as a dopant. While more investigation is required to reveal the role of carbon doping, *in situ* EIS analysis revealed that the presence of doped carbon helps retain the original electrical conductivity and Li^+ diffusivity despite the amorphization. This insight can widen our understanding of the critical factors governing the electrochemical behavior of $TiNb_2O_7$ and help establish a design principle for advanced TNO-based electrode materials.

https://doi.org/10.1021/acsami.2c00589
ACS Appl. Mater. Interfaces 2022, 14, 19365−19375

■ ASSOCIATED CONTENT

Supporting Information

The Supporting Information is available free of charge at https://pubs.acs.org/doi/10.1021/acsami.2c00589.

Additional characterization data including SEM images, Raman spectra, XPS spectra, and postmortem electron microscopic analyses and additional electrochemical analysis results (CV, GITT, and EIS), voltage profiles, and equivalent circuits (PDF)

■ AUTHOR INFORMATION

Corresponding Author

Jin Ho Bang − *Department of Chemical and Molecular Engineering and Department of Applied Chemistry, Center for Bionano Intelligence Education and Research, Hanyang University, Ansan, Gyeonggi-do 15588, Republic of Korea;* orcid.org/0000-0002-6717-3454; Email: jbang@hanyang.ac.kr

Author

Woowon Chung − *Department of Bionano Technology, Hanyang University, Ansan, Gyeonggi-do 15588, Republic of Korea*

Complete contact information is available at: https://pubs.acs.org/10.1021/acsami.2c00589

Notes

The authors declare no competing financial interest.

■ ACKNOWLEDGMENTS

This research was supported by grants from the Basic Science Research Program through the National Research Foundation (NRF) of Korea funded by the Ministry of Science and ICT (NRF-2019R1A2C1003429) and by the Ministry of Education (NRF-2018R1A6A1A03024231).

■ REFERENCES

(1) Melot, B. C.; Tarascon, J. M. Design and Preparation of Materials for Advanced Electrochemical Storage. *Acc. Chem. Res.* **2013**, *46*, 1226−1238.

(2) Brédas, J.-L.; Buriak, J. M.; Caruso, F.; Choi, K.-S.; Korgel, B. A.; Palacín, M. R.; Persson, K.; Reichmanis, E.; Schüth, F.; Seshadri, R.; Ward, M. D. An Electrifying Choice for the 2019 Chemistry Nobel Prize: Goodenough, Whittingham, and Yoshino. *Chem. Mater.* **2019**, *31*, 8577−8581.

(3) Yao, Y.-X.; Yan, C.; Zhang, Q. Emerging Interfacial Chemistry of Graphite Anodes in Lithium-Ion Batteries. *Chem. Commun.* **2020**, *56*, 14570−14584.

(4) Thackeray, M. M.; Amine, K. $Li_4Ti_5O_{12}$ Spinel Anodes. *Nat. Energy* **2021**, *6*, 683−683.

(5) Lim, H.; Abbas, M. A.; Bang, J. H. Memory Effect in Lithium Titanate Driven by Interfacial Oxygen Vacancies. *ACS Energy Lett.* **2022**, *7*, 1086−1091.

(6) Han, J.-T.; Huang, Y.-H.; Goodenough, J. B. New Anode Framework for Rechargeable Lithium Batteries. *Chem. Mater.* **2011**, *23*, 2027−2029.

(7) Han, J.-T.; Goodenough, J. B. 3-V Full Cell Performance of Anode Framework $TiNb_2O_7$/Spinel $LiNi_{0.5}Mn_{1.5}O_4$. *Chem. Mater.* **2011**, *23*, 3404−3407.

(8) Wang, H.; Qian, R.; Cheng, Y.; Wu, H.-H.; Wu, X.; Pan, K.; Zhang, Q. Micro/Nanostructured $TiNb_2O_7$-Related Electrode Materials for High-Performance Electrochemical Energy Storage: Recent Advances and Future Prospects. *J. Mater. Chem. A* **2020**, *8*, 18425−18463.

(9) Griffith, K. J.; Harada, Y.; Egusa, S.; Ribas, R. M.; Monteiro, R. S.; Von Dreele, R. B.; Cheetham, A. K.; Cava, R. J.; Grey, C. P.; Goodenough, J. B. Titanium Niobium Oxide: From Discovery to Application in Fast-Charging Lithium-Ion Batteries. *Chem. Mater.* **2021**, *33*, 4−18.

(10) Lee, J.; Kwak, H. H.; Bak, S.-e.; Lee, G. J.; Hong, S.-T.; Abbas, M. A.; Bang, J. H. New Class of Titanium Niobium Oxide for a Li-Ion Host: $TiNbO_4$ with Purely Single-Phase Lithium Intercalation. *Chem. Mater.* **2022**, *34*, 854−863.

(11) Griffith, K. J.; Wiaderek, K. M.; Cibin, G.; Marbella, L. E.; Grey, C. P. Niobium Tungsten Oxides for High-Rate Lithium-Ion Energy Storage. *Nature* **2018**, *559*, 556−563.

(12) Kim, Y.; Jacquet, Q.; Griffith, K. J.; Lee, J.; Dey, S.; Rinkel, B. L. D.; Grey, C. P. High Rate Lithium Ion Battery with Niobium Tungsten Oxide Anode. *J. Electrochem. Soc.* **2021**, *168*, No. 010525.

(13) Griffith, K. J.; Seymour, I. D.; Hope, M. A.; Butala, M. M.; Lamontagne, L. K.; Preefer, M. B.; Koçer, C. P.; Henkelman, G.; Morris, A. J.; Cliffe, M. J.; Dutton, S. E.; Grey, C. P. Ionic and Electronic Conduction in $TiNb_2O_7$. *J. Am. Chem. Soc.* **2019**, *141*, 16706−16725.

(14) Griffith, K. J.; Forse, A. C.; Griffin, J. M.; Grey, C. P. High-Rate Intercalation without Nanostructuring in Metastable Nb_2O_5 Bronze Phases. *J. Am. Chem. Soc.* **2016**, *138*, 8888−8899.

(15) Lou, S.; Cheng, X.; Zhao, Y.; Lushington, A.; Gao, J.; Li, Q.; Zuo, P.; Wang, B.; Gao, Y.; Ma, Y.; Du, C.; Yin, G.; Sun, X. Superior Performance of Ordered Macroporous $TiNb_2O_7$ Anodes for Lithium Ion Batteries: Understanding from the Structural and Pseudocapacitive Insights on Achieving High Rate Capability. *Nano Energy* **2017**, *34*, 15−25.

(16) Lee, L.; Kang, B.; Han, S.; Kim, H.-e.; Lee, M. D.; Bang, J. H. A Generalizable Top-Down Nanostructuring Method of Bulk Oxides: Sequential Oxygen−Nitrogen Exchange Reaction. *Small* **2018**, *14*, 1801124.

(17) Voskanyan, A. A.; Abramchuk, M.; Navrotsky, A. Entropy Stabilization of TiO_2−Nb_2O_5 Wadsley−Roth Shear Phases and Their Prospects for Lithium-Ion Battery Anode Materials. *Chem. Mater.* **2020**, *32*, 5301−5308.

(18) Inada, R.; Kumasaka, R.; Inabe, S.; Tojo, T.; Sakurai, Y. Li^+ Insertion/Extraction Properties for $TiNb_2O_7$ Single Particle Characterized by a Particle-Current Collector Integrated Microelectrode. *J. Electrochem. Soc.* **2018**, *166*, A5157−A5162.

(19) Catti, M.; Pinus, I.; Knight, K. Lithium Insertion Properties of $Li_xTiNb_2O_7$ Investigated by Neutron Diffraction and First-Principles Modelling. *J. Solid State Chem.* **2015**, *229*, 19−25.

(20) Xu, Z.; Rahman, M. M.; Mu, L.; Liu, Y.; Lin, F. Chemomechanical Behaviors of Layered Cathode Materials in Alkali Metal Ion Batteries. *J. Mater. Chem. A* **2018**, *6*, 21859−21884.

(21) Lee, G. J.; Abbas, M. A.; Bang, J. H. Pillar Effect in Ni-Rich Cathode of Li-Ion Battery by NH_3 Thermal Treatment. *Bull. Korean Chem. Soc.* **2021**, *42*, 934−937.

(22) Niida, H.; Takahashi, M.; Uchino, T.; Yoko, T. Preparation and Structure of Organic−Inorganic Hybrid Precursors for New Type Low-Melting Glasses. *J. Non-Cryst. Solids* **2002**, *306*, 292−299.

(23) Lee, E. J.; Nam, I.; Yi, J.; Bang, J. H. Nanoporous Hexagonal TiO_2 Superstructure as a Multifunctional Material for Energy Conversion and Storage. *J. Mater. Chem. A* **2015**, *3*, 3500−3510.

(24) Hwang, C. H.; Kim, H.-e.; Nam, I.; Bang, J. H. Polygonal Multi-Polymorphed $Li_4Ti_5O_{12}$@Rutile TiO_2 as Anodes in Lithium-Ion Batteries. *Nano Res.* **2019**, *12*, 897−904.

(25) Choi, W. H.; Lee, C. H.; Kim, H.-e.; Lee, S. U.; Bang, J. H. Designing a High-Performance Nitrogen-Doped Titanium Dioxide Anode Material for Lithium-Ion Batteries by Unravelling the Nitrogen Doping Effect. *Nano Energy* **2020**, *74*, 104829.

(26) Yu, L.; Han, R.; Sang, X.; Liu, J.; Thomas, M. P.; Hudak, B. M.; Patel, A.; Page, K.; Guiton, B. S. Shell-Induced Ostwald Ripening: Simultaneous Structure, Composition, and Morphology Transformations During the Creation of Hollow Iron Oxide Nanocapsules. *ACS Nano* **2018**, *12*, 9051−9059.

(27) Takase, K.; Nishizawa, H.; Onda, A.; Yanagisawa, K.; Yin, S. Synthesis and Characterization of Glycolate Precursors to $MTiO_3$ ($M=Ni^{2+}$, Co^{2+}, Zn^{2+}). *J. Asian Ceram. Soc.* **2017**, *5*, 482−488.
(28) Yang, Y.; Yue, Y.; Wang, L.; Cheng, X.; Hu, Y.; Yang, Z.-z.; Zhang, R.; Jin, B.; Sun, R. Facile Synthesis of Mesoporous $TiNb_2O_7$/C Microspheres as Long-Life and High-Power Anodes for Lithium-Ion Batteries. *Int. J. Hydrogen Energy* **2020**, *45*, 12583−12592.
(29) Yan, C.; Chen, G.; Zhou, X.; Sun, J.; Lv, C. Template-Based Engineering of Carbon-Doped Co_3O_4 Hollow Nanofibers as Anode Materials for Lithium-Ion Batteries. *Adv. Funct. Mater.* **2016**, *26*, 1428−1436.
(30) Yan, C.; Zhu, Y.; Li, Y.; Fang, Z.; Peng, L.; Zhou, X.; Chen, G.; Yu, G. Local Built-in Electric Field Enabled in Carbon-Doped Co_3O_4 Nanocrystals for Superior Lithium-Ion Storage. *Adv. Funct. Mater.* **2018**, *28*, 1705951.
(31) Goriparti, S.; Miele, E.; Prato, M.; Scarpellini, A.; Marras, S.; Monaco, S.; Toma, A.; Messina, G. C.; Alabastri, A.; Angelis, F. D.; Manna, L.; Capiglia, C.; Zaccaria, R. P. Direct Synthesis of Carbon-Doped TiO_2−Bronze Nanowires as Anode Materials for High Performance Lithium-Ion Batteries. *ACS Appl. Mater. Interfaces* **2015**, *7*, 25139−25146.
(32) Guo, B.; Yu, X.; Sun, X.-G.; Chi, M.; Qiao, Z.-A.; Liu, J.; Hu, Y.-S.; Yang, X.-Q.; Goodenough, J. B.; Dai, S. A Long-Life Lithium-Ion Battery with a Highly Porous $TiNb_2O_7$ Anode for Large-Scale Electrical Energy Storage. *Energy Environ. Sci.* **2014**, *7*, 2220−2226.
(33) Lee, G. J.; Abbas, M. A.; Lee, M. D.; Lee, J.; Lee, J.; Bang, J. H. Lithiation Mechanism Change Driven by Thermally Induced Grain Fining and Its Impact on the Performance of $LiMn_2O_4$ in Lithium-Ion Batteries. *Small* **2020**, *16*, 2002292.
(34) Ha, J. U.; Lee, J.; Abbas, M. A.; Lee, M. D.; Lee, J.; Bang, J. H. Designing Hierarchical Assembly of Carbon-Coated TiO_2 Nanocrystals and Unraveling the Role of TiO_2/Carbon Interface in Lithium-Ion Storage in TiO_2. *ACS Appl. Mater. Interfaces* **2019**, *11*, 11391−11402.
(35) Come, J.; Augustyn, V.; Kim, J. W.; Rozier, P.; Taberna, P.-L.; Gogotsi, P.; Long, J. W.; Dunn, B.; Simon, P. Electrochemical Kinetics of Nanostructured Nb_2O_5 Electrodes. *J. Electrochem. Soc.* **2014**, *161*, A718−A725.
(36) Cava, R. J.; Murphy, D. W.; Zahurak, S. M. Lithium Insertion in Wadsley-Roth Phases Based on Niobium Oxide. *J. Electrochem. Soc.* **1983**, *130*, 2345−2351.
(37) Wu, X.; Lou, S.; Cheng, X.; Lin, C.; Gao, J.; Ma, Y.; Zuo, P.; Du, C.; Gao, Y.; Yin, G. Unravelling the Interface Layer Formation and Gas Evolution/Suppression on a $TiNb_2O_7$ Anode for Lithium-Ion Batteries. *ACS Appl. Mater. Interfaces* **2018**, *10*, 27056−27062.
(38) Pender, J. P.; Jha, G.; Youn, D. H.; Ziegler, J. M.; Andoni, I.; Choi, E. J.; Heller, A.; Dunn, B. S.; Weiss, P. S.; Penner, R. M.; Mullins, C. B. Electrode Degradation in Lithium-Ion Batteries. *ACS Nano* **2020**, *14*, 1243−1295.
(39) Li, Y.; Shen, J.; Li, J.; Liu, S.; Yu, D.; Xu, R.; Fu, W.-F.; Lv, X.-J. Constructing a Novel Strategy for Carbon-Doped TiO_2 Multiple-Phase Nanocomposites toward Superior Electrochemical Performance for Lithium Ion Batteries and the Hydrogen Evolution Reaction. *J. Mater. Chem. A* **2017**, *5*, 7055−7063.

https://doi.org/10.1021/acsami.2c00589
ACS Appl. Mater. Interfaces 2022, 14, 19365−19375